



# S-vacancy-rich NiFe-S nanosheets based on a fully electrochemical strategy for large-scale and quasi-industrial OER catalysts

Lixiang He<sup>a</sup>, Ni Wang<sup>a,b,\*</sup>, Mingliang Xiang<sup>a</sup>, Li Zhong<sup>a</sup>, Sridhar Komarneni<sup>b,\*\*</sup>,  
Wencheng Hu<sup>a,\*\*</sup>

<sup>a</sup> School of Materials and Energy, University of Electronic Science & Technology of China, Chengdu 610054, PR China

<sup>b</sup> Materials Research Institute and Department of Ecosystem Science and Management, 204 Energy and the Environment Laboratory, The Pennsylvania State University, University Park, PA 16802, USA

## ARTICLE INFO

### Keywords:

Oxygen evolution reaction (OER)  
Sulfur vacancy  
Electrochemical reduction  
Industrial application  
DFT calculation

## ABSTRACT

The oxygen evolution reaction (OER) is regarded as a critical component in the water splitting system. Creating vacancies, increasing active surface area, and optimizing electronic structure would improve electrocatalytic performance. Herein, a facile electrochemical reduction method is used to generate sulfur vacancies in nickel iron sulfide (NiFe-S) with a large geometry area of  $15 \times 16 \text{ cm}^2$ , which is synthesized using an electrodeposition process assisted with the ion exchange (IOE) method. The X-ray absorption spectroscopies (XAS) are applied for atomic-level structural analysis, verifying that electrochemical desulfurization generates abundant S vacancies. The NiFe-S with abundant sulfur vacancies (NiFe-S-V<sub>s</sub>) exhibits a low overpotential (252 mV at  $100 \text{ mA cm}^{-2}$ ), and long stability for 260 h at  $500 \text{ mA cm}^{-2}$ . More importantly, the NiFe-S-V<sub>s</sub> catalyst also delivers a small overpotential (235 mV at  $1000 \text{ mA cm}^{-2}$ ) and high alkaline tolerance (140 h at  $500 \text{ mA cm}^{-2}$ ) in 6 M KOH at  $60^\circ\text{C}$ , implying a potentially significant industrial application prospect. Finally, theory calculation further illustrates the high performance of as-prepared vacancies-rich catalyst.

## 1. Introduction

Air pollution and greenhouse gas emissions have posed a serious threat to human health around the world. The demand for low or even zero carbon emissions is increasing constantly for vehicles and industries, which is driving new energy sources to the fore front leading to a new green energy boom. Renewable solar, wind, tidal, and geothermal are inexhaustible natural resources on the earth. Unfortunately, these energies are discontinuous and uncontrollable, necessitating the use of energy storage methods [1,2]. Hydrogen is regarded as a strong candidate owing to its nontoxic and environmentally friendly nature along with abundant natural water reserves [3]. Electrolysis of water to generate hydrogen is a promising approach for producing unlimited energy sources without CO<sub>2</sub> emissions. The water electrolysis reaction includes the hydrogen evolution reaction (HER) at the cathode and the oxygen evolution reaction (OER) at the anode. Both HER and OER are endergonic reactions in terms of thermodynamics, and the reaction requires a theoretical voltage of 1.23 V. Due to a kinetic barrier in the

electrolysis process, an additional overpotential is required to achieve water splitting [4]. Furthermore, the OER, as a four-electron-transfer reaction, incorporates sluggish loss-of-electron elementary reactions in water electrolysis based on dynamics. The slow kinetics and complicated mechanisms of the OER have limited large-scale application of hydrogen production via water electrolysis [5]. Besides, OER is an important reaction in rechargeable metal-air batteries, and the high overpotential results in low energy efficiency [6]. On the other hand, industrial water splitting electrocatalysts should have several distinguishing characteristics, including high intrinsic activity, a large surface area for exposing many active sites, outstanding conductivity, excellent durability, and good stability under high current density ( $>500 \text{ mA cm}^{-2}$ ), high temperature ( $60\text{--}80^\circ\text{C}$ ), and high alkaline concentration (20–30 wt% KOH) [7]. Unfortunately, there aren't many electrocatalysts that can meet these stringent requirements, and most researchers are focused on the microscopic and intrinsic properties of the material rather than its application. As a result, it is critical to develop efficient electrocatalysts for OER to seriously reach the practical application state.

\* Corresponding author at: School of Materials and Energy, University of Electronic Science & Technology of China, Chengdu 610054, PR China.

\*\* Corresponding authors.

E-mail addresses: [niwang@uestc.edu.cn](mailto:niwang@uestc.edu.cn) (N. Wang), [sxk7@psu.edu](mailto:sxk7@psu.edu) (S. Komarneni), [huwc@uestc.edu.cn](mailto:huwc@uestc.edu.cn) (W. Hu).

<https://doi.org/10.1016/j.apcatb.2023.123686>

Received 22 October 2023; Received in revised form 14 December 2023; Accepted 30 December 2023

Available online 4 January 2024

0926-3373/© 2023 Elsevier B.V. All rights reserved.

In general, noble metal-based catalysts such as  $\text{IrO}_2$  and  $\text{RuO}_2$  have excellent performance for OER located near the peak of volcano plots [8]. However, the stability of noble metal-based catalysts is very poor at high potential, whereas the intrinsic advantages of transition metal-based catalysts, such as cost-effectiveness, high earth abundance, and adjustable electron structure, increase the possibility of large-scale application [9]. In addition, transition metal-based electrocatalysts with 3d orbit are similar to noble metal-based catalysts, which stimulates researchers' interest. In alkaline conditions, nickel oxides [10] or hydroxides [11] have demonstrated excellent catalytic activity for OER. Furthermore, the presence of second metal elements such as Fe [12], Co [13], Mn [14], etc. can boost the activity of nickel oxides or hydroxides. It has been demonstrated that NiFe-based (oxy)hydroxides have the lowest overpotential among several ternary metal-based catalysts [15] and even have higher activity than  $\text{IrO}_2$  electrocatalysts [16]. More importantly, the cost of the Fe element is not only lower, but it is also non-toxic, and its content is the highest among transition elements in the earth's crust. However, the conductivity of NiFe-based (oxy)hydroxides is inadequate, preventing this type of catalyst from improving OER performance. Hence, catalysts are generally fabricated on metal or carbon substrates to improve conductivity or avoid the use of expensive conductive polymeric binders [17]. Because of the good conductivity and 3D structure of nickel foam, it is frequently used as catalyst support. Other types of transition metal compounds, such as sulfides [18], nitrides [19], phosphides [20], selenides [21], carbides [22], and others, have emerged in the field of efficient water splitting in recent years. Sulfides, in particular, are extremely active for OER. Furthermore, metal sulfides are a mineral class [23], so there are significant advantages of rich resources and low prices that make industrial applications possible.

Transition metal chalcogenides are also proposed as pre-catalysts. It has been proved that pre-catalysts have superior electrochemical performance and electrical conductivity [24]. When sulfides or other compounds on the surface of pre-catalysts are oxidized and transformed into corresponding oxides and (oxy)hydroxides [25], it was demonstrated that the reconstructed oxides and (oxy)hydroxides are real active moieties [26]. More importantly, surface reconstructed moieties have been shown to have higher activity for OER than directly synthesized metal oxides and (oxy)hydroxides [27]. Optimizing the electronic structures of electrocatalysts, particularly the introduction of vacancies, is commonly used to further improve the OER performance of catalysts. By forming new gap states and defects, the generation of S vacancies can improve conductivity and increase the exposure of active sites on the surface of the catalyst [28]. At present, many works are focused on sulfur vacancies of molybdenum-based [29] and nickel-cobalt-based [30] sulfide electrocatalysts but little attention has been paid to introducing sulfur vacancies into NiFe-S electrocatalysts for water electrolysis. Numerous strategies have been utilized to create vacancies. However, there are a few reports that adopt sulfur vacancies to improve electrochemical OER. Vacancy engineering commonly includes plasma etching [31], thermal treatment [32,33], laser fragmentation [34], and wet chemical reduction [35], but most of them are energy intensive and difficult to scale up, and security risks are unavoidable due to the use of flammable and explosive gases. On the contrary, chemical reduction and electrochemical treatment are simpler, more energy-efficient, and more scalable techniques, particularly electrochemical treatment. While the reduction ability of commonly used chemical reagents such as  $\text{NaBH}_4$  and  $\text{NH}_2\text{NH}_2$  is well-known, the reduction process may produce potentially hazardous gases due to the decomposition of chemical reducers while creating vacancies. The reduction ability of the electrochemical method can be directly determined by the controlled cathode potential only using a direct-current power supply, which is a simple, stable, easy-to-operate, and low-cost method. Only a few studies have focused on this method of creating anionic vacancies. It is very important to use electrochemical treatment to generate vacancies in NiFe-S electrocatalysts for water splitting because of the disadvantages associated with chemical reducers. We know that the reduction reaction can occur at the

cathode of an electrolytic cell, and the reduction capacity can be controlled by the potential applied to the cathode.

Based on the above reasons, herein we provide a facile route to synthesize excellent water splitting electrocatalysts with a large area by a three-step approach. Firstly, the NiFe LDH supported on NF (NiFe LDH/NF) has been synthesized through a typical LDH synthesis method of constant voltage electrodeposition. The NiFe-LDH/NF precursor was then sulfurized using ion exchange (IOE) to prepare NiFe-S/NF. In order to further improve the activity of the catalyst, a facile electrochemical method was used to generate sulfide vacancies and adjust its electronic structure. Furthermore, under industrial water electrolysis conditions, the potential for industrial application has been investigated. The results show that the NiFe-S/NF with sulfur vacancies, i.e., NiFe-S- $\text{V}_\text{s}$ /NF sample has increased activity and holds great promise for industrial electrolysis of water on a large scale.

## 2. Experimental section

### 2.1. Materials

Acetone ( $\text{C}_3\text{H}_6\text{O}$ , AR, 99.5%), ethanol ( $\text{C}_2\text{H}_5\text{OH}$ , GR, 99.7%), HCl (AR, 36–38%),  $\text{Ni}(\text{NO}_3)_2 \cdot 6\text{H}_2\text{O}$  (AR, 98.5%),  $\text{Fe}(\text{NO}_3)_3 \cdot 9\text{H}_2\text{O}$  (AR, 99%),  $\text{Na}_2\text{S}$  (AR, 98%), and KOH (AR, 95%) were all purchased from Chengdu Kelong Reagent Co., Ltd. and not purified further. Deionized water was manufactured through a pure water meter (Sichuan Jinlan Technology Co., Ltd.).

### 2.2. Synthesis of NiFe-LDH/NF

Some pieces of Ni foam ( $1 \times 2\text{ cm}^2$ ) were ultrasonically cleaned in deionized water, acetone, ethanol, and 3 M HCl solution for 20 min, respectively. The Ni foam was then washed several times with deionized water and vacuum dried at  $60^\circ\text{C}$  for 24 h. The NiFe-LDH nanosheets were synthesized on NF via electrodeposition in a three-electrode system. The working electrode is NF, the counter electrode is Pt foil, and the reference electrode is Ag/AgCl electrode. The electrolyte contained 5 mM  $\text{Ni}(\text{NO}_3)_2 \cdot 6\text{H}_2\text{O}$  and 10 mM  $\text{Fe}(\text{NO}_3)_3 \cdot 9\text{H}_2\text{O}$ , and the experiments were conducted using constant potential electrodeposition for 600 s at  $-1.0\text{ V}$  vs. Ag/AgCl electrode. The as-prepared NiFe-LDH/NF precursors were washed several times with DI water and dried overnight at  $60^\circ\text{C}$ .

### 2.3. Synthesis of NiFe-S/NF

In a typical sulfurization process of NiFe-LDH/NF precursors, 80 mL of 1 M  $\text{Na}_2\text{S}$  solution was prepared and heated to  $80^\circ\text{C}$ , then NiFe-LDH/NF precursors were immersed in it for 8 h. Following that, the sulfurized samples were repeatedly cleaned with DI water and dried in a vacuum at  $60^\circ\text{C}$  for 10 h.

### 2.4. Synthesis of NiFe-S- $\text{V}_\text{s}$ /NF

Here, a facile electrochemical method was applied to generate sulfide vacancies. Constant voltage reduction was carried out in an electrochemical cell using the prepared NiFe-S/NF sample as a cathode and Pt mesh as an anode, with 1 M KOH solution serving as the electrolyte for 2 h. The applied voltage is then adjusted to 0.2 V, 0.4 V, 0.6 V, 0.8 V, and 1.0 V, and the resulting vacancy-rich samples are designated as NiFe-S-0.2/NF, NiFe-S-0.4/NF, NiFe-S-0.6/NF, NiFe-S-0.8/NF, and NiFe-S-1.0/NF, respectively.

### 2.5. Material characterization

SEM (Inspect F, FEI Co., US, 15 kV) was used to represent the microstructure of as-synthesized materials, and EDS and mapping were adopted to analyze elementary contents and distribution. TEM (Libra

200FE, Germany, 200 kV) was also used to confirm the structure. To characterize the crystal structure and crystallinity, an XRD (Bruker D8 advance, Germany, 40 mA, 40 kV) was used with a scanning range from  $10^\circ$  to  $90^\circ$ . XPS (XSAM800, Kratos, 15 kV, 10 mA, 40 eV) with Al K $\alpha$  ray was employed to investigate the valence states of elements. Raman spectrum was applied by Renishaw (invia, U.K.). The X-ray absorption spectroscopies (XAS) at Fe and Ni K-edge were collected using the X-ray absorption fine structure (XAFS) station of the Shanghai Synchrotron Radiation Facility (SSRF), Anhui Absorption Spectroscopy Analysis instrument Co.Ltd. of RapidXAFS 1 M, and Hefei National Synchrotron Radiation Laboratory (NSRL). X-ray absorption near edge structure (XANES) and extended X-ray absorption fine structure (EXAFS) data were analyzed using the ATHENA program [36]. To confirm the presence of vacancies, EPR measurements were performed at room temperature on an EMX Plus (Bruker EMXnano, Germany, 9.60 GHz, 3.162 mW).

## 2.6. Electrochemical measurements

An electrochemical station (SCS) with a standard three-electrode system was employed to perform electrochemical measurements. In an alkaline medium, the as-prepared samples were used as work electrodes directly, while platinum films and Hg/HgO electrodes were used as

counter and reference electrodes. The CV curves were measured to active catalysts for the OER measurement. Initially, linear sweep voltammetry (LSV) at a scanning rate of  $1 \text{ mV s}^{-1}$  was obtained, and Tafel slopes were calculated by fitting the Tafel plots according to the Tafel formula ( $\eta = a + b \log |j|$ ). Electrochemical impedance spectroscopy (EIS) was carried out from 0.01 Hz to 100 kHz at an overpotential of 50 mV. The electrochemical active surface area (ECSA) was gained by fitting the CV area with different scanning rates at a non-Faradaic potential window. The durability tests were carried out in a LANHE test system (LAND, CT2001A, China) at  $500 \text{ mA cm}^{-2}$ . Furthermore, electrochemical measurements were performed at room temperature,  $60^\circ\text{C}$ ,  $70^\circ\text{C}$ , and  $80^\circ\text{C}$  in 1 M KOH and 6 M KOH respectively. All potentials of LSV curves were referenced to a reversible hydrogen electrode (RHE):  $E_{\text{RHE}} = E_{(\text{Hg}/\text{HgO})} + 0.059 \text{ pH} + 0.098 \text{ V}$  with 90% iR compensation. And the overpotential is calculated by  $E_{\text{RHE}} = \eta + 1.23 \text{ V}$ .

## 3. Results and discussion

### 3.1. Materials synthesis and characterization

The specific synthesis process for NiFe-S-0.6/NF nanosheets is illustrated in Fig. 1a. As shown in Fig. S1, the color of NF becomes brown after the first electrodeposition, suggesting that NiFe-LDH has been

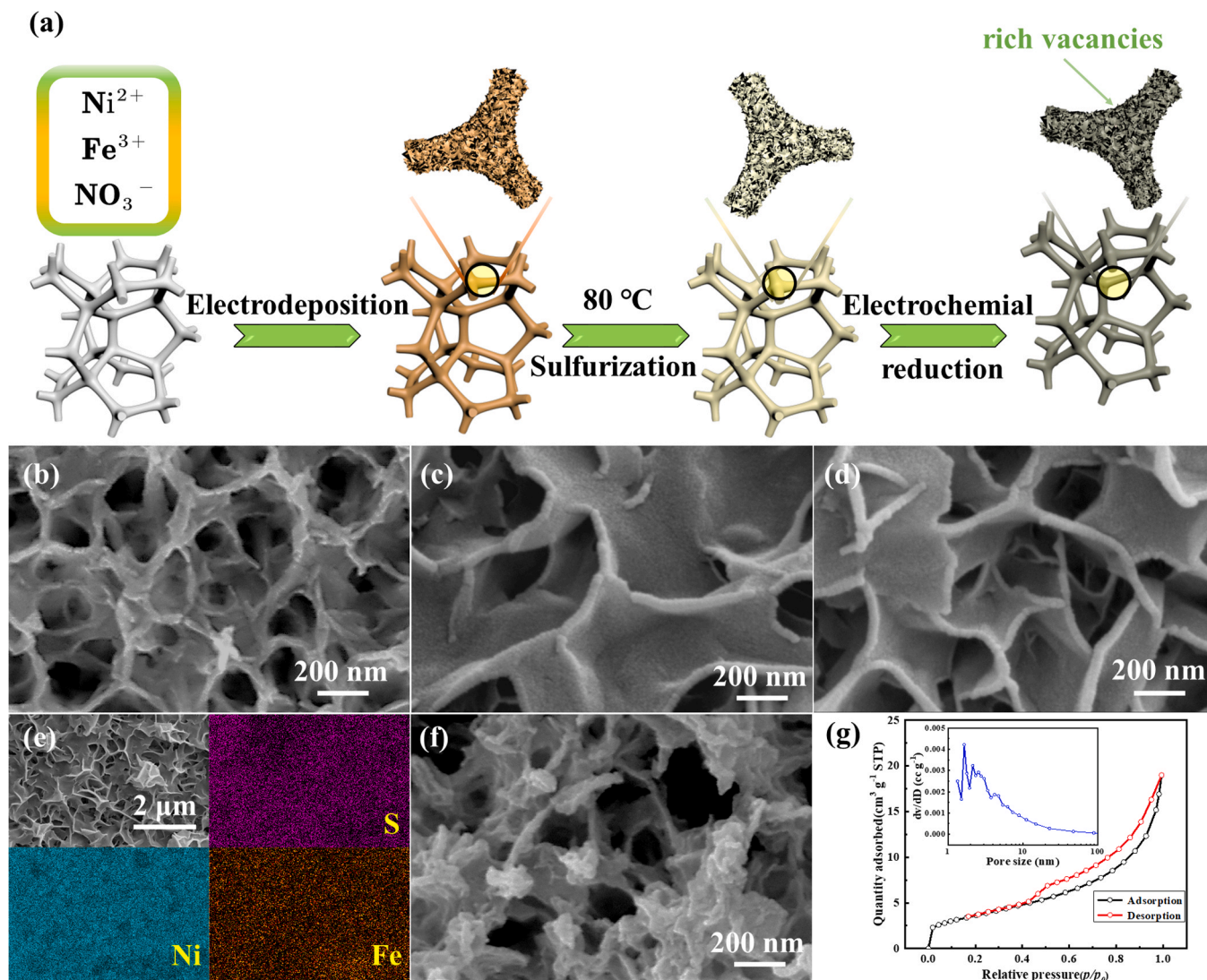


**Fig. 1.** (a) Schematic diagram of the synthesis of NiFe-LDH/NF, NiFe-S/NF, and NiFe-S-Vs/NF electrodes, SEM image of (b) NiFe-LDH/NF, (c) NiFe-S/NF, (d) NiFe-S-0.6/NF, (e) SEM and EDS element mapping of NiFe-S-0.6/NF, (f) SEM of long-time OER tested NiFe-S-0.6/NF and (g) BET of NiFe-S-0.6/NF.



synthesized, and the brown color changed to black as a result of sulfide formation via a typical anion exchange reaction. Finally, the rich-vacancy sulfide was synthesized by the facile electrochemical reduction process and after reduction, the color still stays black. The morphological features of NiFe-LDH, NiFe-S/NF, and NiFe-S-0.6/NF were revealed by SEM. As shown in Fig. 1b, NiFe-LDH was synthesized with a nanosheet structure. The NiFe-S/NF precursors were successfully prepared from the NiFe-LDH nanosheets, and the nanosheet structure was well maintained after the sulfurization process as shown in Fig. 1c. Moreover, according to Fig. 1d, the electrochemical reduction did not have much effect on the morphology and the nanosheet shape of the initial NiFe-LDH sample could be maintained. The nanosheets with different sizes were grown irregularly on NF, which not only provides a large specific surface between the electrolyte solution and active material, exposing more active sites for the electrochemical reaction but also helps to release the gas. EDS with elemental mappings of NiFe-S-0.6, as shown in Fig. 1e, indicates a uniform distribution of S, Ni, and Fe elements on the nanosheets. EDS spectra of NiFe-S and NiFe-S-0.6 are shown in Fig. S4a, b, where the three elements also can be found. The  $N_2$  adsorption-desorption isotherms are shown in Fig. 1g, which display a typical type IV category according to the Brunauer–Deming–Teller classification revealing that the sample possesses a mesoporous characteristic [37]. The BET specific surface area of NiFe-S-0.6/NF is calculated to be  $13.16 \text{ m}^2 \text{ g}^{-1}$ . To investigate the effect of reduction potential on materials, SEM images of samples treated with different potentials are demonstrated in Fig. S2 at low-magnification and in Fig. S3 at high-magnification. It is found that the micro-morphology of materials did not change under different applied voltages, but the surface of nanosheets is not smooth in all samples. Only a minor difference in thickness is discovered in the NiFe-S-1.0 sample, indicating that the effect of applied voltage on catalyst morphology is insignificant.

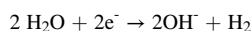
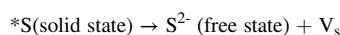
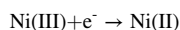
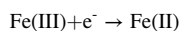
TEM was used to observe the morphology and structure of NiFe-S-0.6 in greater detail (Fig. 2). The TEM image further corroborates that NiFe-S-0.6 possesses uniformly thick nanosheets with 3D structure (Fig. 2a). Numerous lattice fringes are obvious in the HRTEM image of NiFe-0.6 nanosheets and the interplanar spacings are 0.17 nm, 0.18 nm, 0.23 nm, and 0.28 nm, which can be related to both the (121), (120), (111), ( $\bar{1}10$ ) crystal planes for  $\text{Ni}_3\text{S}_2$  and (440), (511), (400) and (311) crystal planes for  $(\text{Fe}, \text{Ni})_3\text{S}_4$ , respectively (Fig. 2b). There are also amorphous regions as revealed in the upper right corner of Fig. 2b. It is worth noting that not all lattice fringes are continuous and many dislocations or distortions exist in the NiFe-S-0.6, as seen in the dotted frame of Fig. 2c, but not just limited to these regions, suggesting a large number of defects are present in the as-prepared catalysts, which is favorable to the high content of active sites and a more reasonable electronic structure [38]. In Fig. S5, we can see an enlarged view of two defective areas, from which we can clearly see where the atom is missing or where the lattice misalignment is. This means that electrochemical reduction is an efficient method for producing abundant defects. Furthermore, the selected area electron diffraction (SAED) exhibits a series of diffraction rings, corresponding to ( $\bar{1}10$ ), (111), (120), ( $\bar{1}21$ ) lattice planes of  $\text{Ni}_3\text{S}_2$ , and (311), (400), (511) lattice planes of  $(\text{Fe}, \text{Ni})_3\text{S}_4$  (Fig. 2d). After 260 h of Chronopotentiometry at a constant current density of  $500 \text{ mA cm}^{-2}$ , the nanosheet structure can still be maintained, as shown in Fig. S6a, suggesting strong stability of the vacancy-rich NiFe-S-0.6 electrocatalyst. The nanosheet structure has been maintained and the nanosheets appear to have grown after a long-term test (Fig. S6a), which may be because part of the sulfide precatalyst changed to hydroxides on the surface. And the elements mapping is displayed in Fig. S6b, where the Ni, Fe, S, and O are distributed on the nanosheet and the S elements are mainly concentrated in the middle region of the nanosheet, suggesting the formation of hydroxysulfides. From HRTEM shown in Fig. S6c, it can be seen that there is an amorphous layer outside and apparent lattice fringes in the inner layer, whose interplanar spaces have altered to 0.199 nm, and 0.234 nm, which are greatly different from the original vacancy-rich

material. The same situation is revealed in SAED (Fig. S6e). Significantly, large-scale lattice fringes are missing, but dislocations and distortions also exist (Fig. S6d). All of these HRTEM observations hinted that the catalyst and its crystal structure have changed.

X-ray diffraction (XRD) is used to confirm the crystal structure and phase information of materials. As displayed in Fig. 2e, the NiFe-S-0.6/NF and NiFe-S/NF exhibit strong diffraction peaks at  $44.3^\circ$ ,  $51.7^\circ$ , and  $76.3^\circ$  originated from Ni foam (JCPDS No. 87–0712) of the substrate. The weak peaks at  $21.9^\circ$ ,  $31.2^\circ$ ,  $38.1^\circ$ ,  $44.1^\circ$ ,  $50.2^\circ$ , and  $55.5^\circ$  can be indexed as the (010), ( $\bar{1}10$ ), (111), (020), (120), and (121) planes of  $\text{Ni}_3\text{S}_2$  (JCPDS No. 71–1682), while the peaks at  $26.5^\circ$ ,  $31.2^\circ$ ,  $38.1^\circ$ ,  $50.2^\circ$  and  $55.5^\circ$  can be assigned to the (220), (311), (400), (511) and (440) planes of  $(\text{Fe}, \text{Ni})_3\text{S}_4$  (JCPDS No. 11–0095) and these XRD results are consistent with the HRTEM and SAED results of a mixture of  $\text{Ni}_3\text{S}_2$  and  $(\text{Fe}, \text{Ni})_3\text{S}_4$ . In addition, the distinct shift to a lower angle of the above peaks indicates (inset of Fig. 2e) the existence of sulfur vacancies after electrochemical reduction [39].

In the EPR spectra (Fig. 2f), NiFe-S-0.6 shows abundant  $V_s$  with a stronger EPR signal intensity at  $g = 2.003$  compared to NiFe-S. The wide peak at approximately 3500 Gauss in both samples can be attributed to magnetism caused by unpaired electrons [40], where the intensity is considered to be proportional to the quantity of M-S unsaturated dangling bonds from  $V_s$  [41]. To obtain more insight into the nature of the vacancies, Raman spectroscopies for a set of sulfides reduced at different potentials were determined, as shown in Fig. 2g. The four obvious peaks of NiFe-S catalysts at  $346 \text{ cm}^{-1}$ ,  $473 \text{ cm}^{-1}$ ,  $531 \text{ cm}^{-1}$ , and  $672 \text{ cm}^{-1}$  correspond to  $E_g$ ,  $T_{2g}$ ,  $F_{2g}$ , and  $A_{1g}$ , respectively [42,43]. Significantly, the Raman scattering peaks have a blue shift to a higher frequency as the voltage for electrochemical reduction increased, further indicating the existence of  $V_s$  [30]. The results of XRD, EPR, and Raman demonstrate that the defects shown in TEM are mainly sulfur vacancies.

We postulate the mechanism of  $V_s$  formation process, and the specific steps at the cathode as follows:



To explore the effect of Fe, Ni, and S elements, and further confirm the generation of  $V_s$ , X-ray photoelectron spectroscopy (XPS) was carried out to differentiate the surface elemental composition and oxidation states. Fig. 3 shows the XPS spectra of Fe 2p, Ni 2p, and S 2p for nickel-iron sulfides without reduction (NiFe-S), NiFe-S-0.6, and NiFe-S-0.6 after 260 h testing. Fig. 3a shows the Fe 2p spectrum, which can be divided into five peaks. The peak at  $715.43 \text{ eV}$  is considered as the satellite peak (abbreviated as “sat.”) and is characterized by the  $\text{Fe}^{2+}$  oxidation state. NiFe-S contains two pairs of spin-orbit peaks with Fe(II) (can be attributed to  $2p_{3/2}$  at  $707.52 \text{ eV}$  and  $2p_{1/2}$  at  $720.12 \text{ eV}$ ) and Fe (III) (can be attributed to  $2p_{3/2}$  at  $711.99 \text{ eV}$  and  $2p_{1/2}$  at  $724.29 \text{ eV}$ ) [44,45]. For NiFe-S samples, peak locations have slightly shifted to the positive direction. In addition, the area ratio of Fe (II):Fe(III) in NiFe-S-0.6 is about 1.97:1, while that in NiFe-S is only 1:1.87. The Ni 2p region of NiFe-S (Fig. 3b) can be deconvoluted with six characteristic peaks, which shows two species of spin-orbit Ni  $2p_{3/2}$  ( $855.05 \text{ eV}$  and  $856.41 \text{ eV}$ ) and Ni  $2p_{1/2}$  ( $872.54 \text{ eV}$  and  $873.90 \text{ eV}$ ), simultaneously along with two satellite peaks (noted as “sat.” at  $861.45 \text{ eV}$  and  $879.29 \text{ eV}$  respectively) assigned to Ni(II) [46]. Moreover, two peaks at  $855.05 \text{ eV}$  for Ni  $2p_{3/2}$  and  $872.54 \text{ eV}$  for Ni  $2p_{1/2}$  indicate the presence of a  $\text{Ni}^{2+}$  oxidation state, while  $856.41 \text{ eV}$  and  $873.90 \text{ eV}$  can be matched to a  $\text{Ni}^{3+}$  oxidation state [47]. Similarly, the Ni 2p spectrum of NiFe-S-0.6 has a little change in the location, while the  $\text{Ni}^{2+}$  and  $\text{Ni}^{3+}$  ratio has altered from 1:0.98 to 1.45:1. Fig. 3c further illustrates the XPS



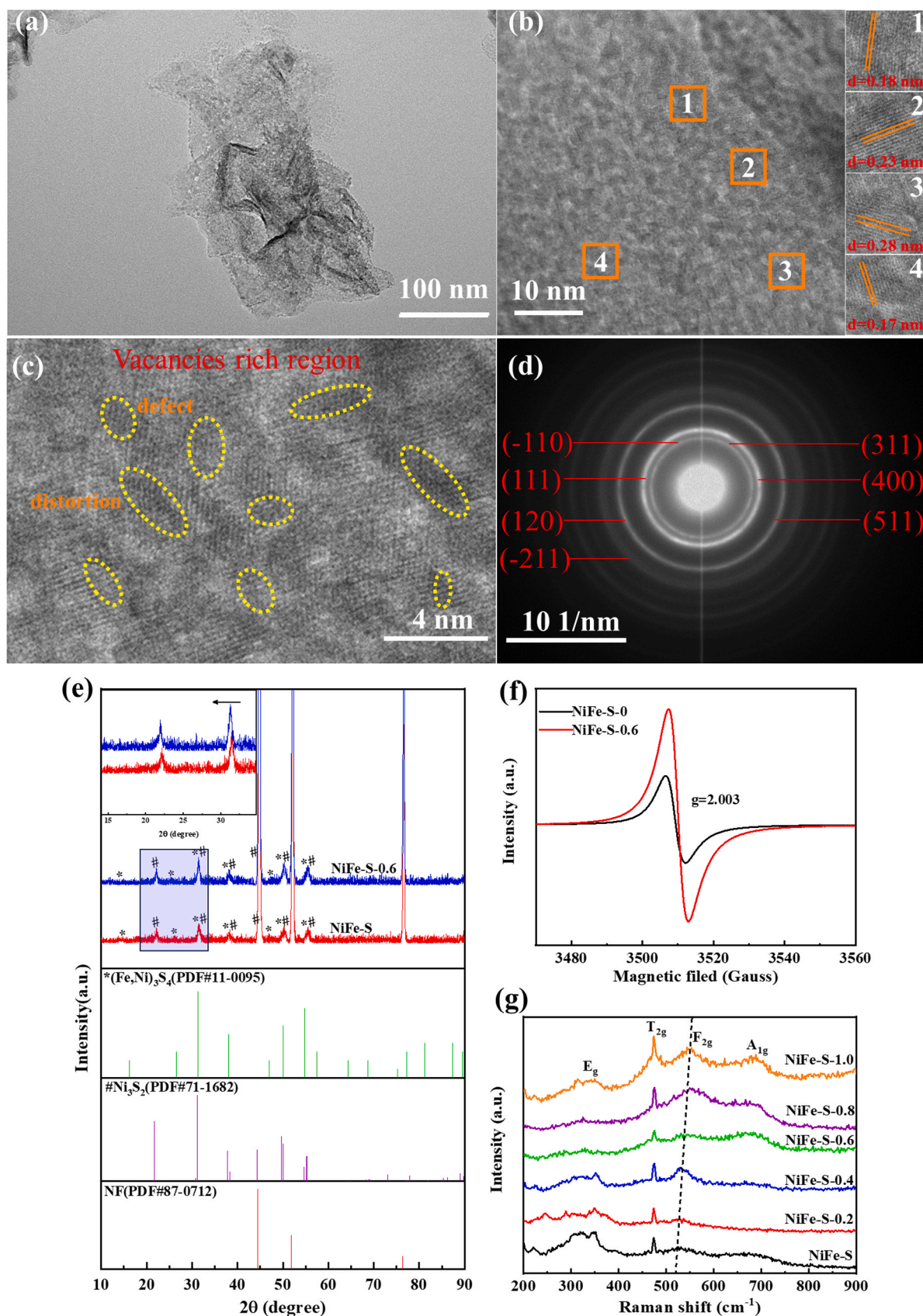


**Fig. 2.** (a) TEM image, (b) HRTEM image, (c) enlarged HRTEM image, (d) SAED pattern of NiFe-S-0.6, (e) XRD patterns of NiFe-S/NF and NiFe-S-0.6/NF (inset: enlargement of the shaded areas), (f) EPR spectra of pristine NiFe-S and rich-vacancies NiFe-S-0.6, and (g) Raman spectra of NiFe-LDH/NF, NiFe-S/NF, NiFe-S-0.2/NF, NiFe-S-0.4/NF, NiFe-S-0.6/NF, NiFe-S-0.8/NF and NiFe-S-1.0/NF.

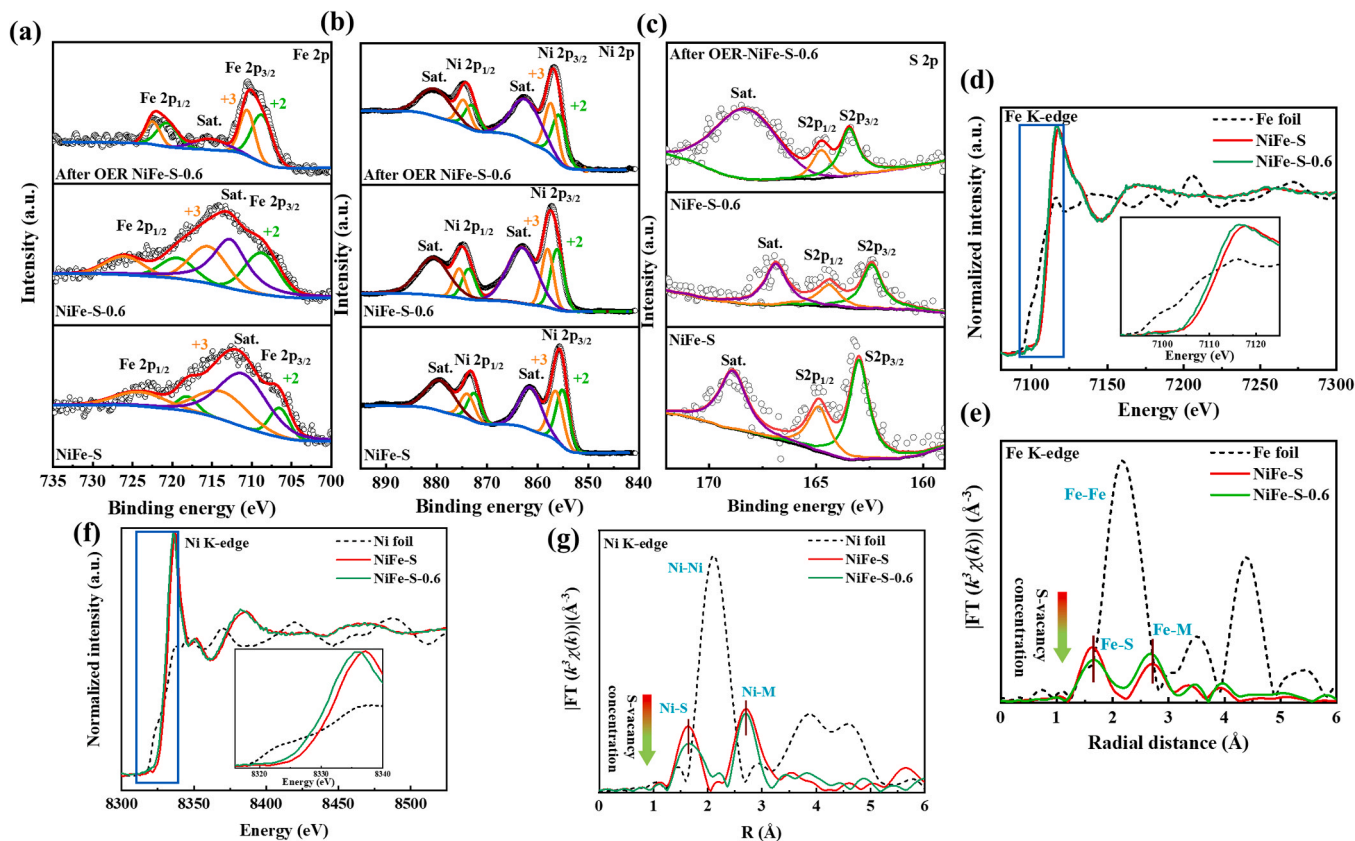


**Fig. 3.** (a–c) XPS spectra on Fe2p, Ni2p, and S2p, of NiFe-S, NiFe-0.6, and after long-term OER tested NiFe-S-0.6; (d) XANES E space spectra and (e) EXAFS R space spectra at the Fe K-edge; (f) XANES E space spectra and (g) EXAFS R space spectra at the Ni K-edge. The insets in (d) and (f) present the enlarged spectra of XANES.

spectrum of S 2p of NiFe-S, where two peaks located at 162.99 eV and 164.88 eV are assigned to S 2p<sub>3/2</sub> and S 2p<sub>1/2</sub> of S<sup>2-</sup> [48,49], and the peak located at 168.90 eV is a satellite peak corresponding to the S oxidation state of nickel iron sulfide on the surface of materials [50,51]. For the NiFe-S-0.6, peaks for S 2p<sub>3/2</sub>, S 2p<sub>1/2</sub>, and “Sta.” have all moved to the negative positions, and the areas of all samples have decreased, indicating the successful generation of sulfur vacancies. Compared to NiFe-S, the amount of + 2 oxidation states for Fe and Ni in NiFe-S-0.6 has increased, further suggesting the high valence transition metals have been reduced to lower valence. This reduction process causes the release of S<sup>2-</sup> from the solid surface of NiFe-S to the solution, resulting in the formation of S vacancies.

X-ray absorption spectroscopy (XAS) measurements were performed to provide a detailed understanding of the coordination environment and chemical states of Fe and Ni in as-prepared catalysts at the atomic level [36]. The X-ray absorption near edge structure (XANES) spectra of NiFe-S, NiFe-S-0.6, and the reference at K-edge are shown in Figs. 3d and 3f. The XANES spectra of Fe K-edge (Fig. 3d) reveal that the NiFe-S-0.6 represents a lower E shift compared with NiFe-S, indicating a lower valence state of Fe in NiFe-S-0.6 (matching to the XPS results in Fig. 3a), which is attributed to the change of electron localization after introducing anion vacancies [52]. Similar results are discovered on the Ni K-edge (Fig. 3f), a negative E shift of NiFe-S-0.6 demonstrates the presence of anionic vacancy and lower valence state with a lower coordination number. The corresponding FT-EXAFS spectra (Fig. 3e, g) reveal that NiFe-S-0.6 demonstrates higher Fe-S and Ni-S bonds (1.67 Å and 1.69 Å, respectively) compared to those of NiFe-S (1.63 Å and 1.65 Å), followed by a reduced bond intensity, suggesting the structure distortion induced by sulfur vacancy [53]. The other prominent peaks at 2.68 Å (NiFe-S-0.6) and 2.70 Å (NiFe-S) correspond to Fe-M bonds at Fe K-edge. Additionally, the markedly increased intensity of the second shell (Fe-M) in NiFe-S-0.6 indicates a significant structural distortion,

demonstrating the existence of S vacancy [54,55]. The fitting results were displayed in Fig. S8, where the reduced coordination numbers and the elongated interatomic distance of Ni-S and Fe-S for NiFe-S-0.6 indicate the existence of S vacancy in catalyst. Similar observations are found in the Ni K-edge FT-EXAFS spectra (Fig. 3g), a slightly longer bond length of Ni-S is owing to the desulfurization after electrochemical reduction. It is obvious that the XAS results clearly support XPS, EPR, and Raman data, confirming the successful fabrication of rich-vacancy nickel-iron sulfides via the facile electrochemical technique.

### 3.2. Electrochemical performance

The OER electrocatalytic performance of as-prepared electrocatalysts was evaluated in an O<sub>2</sub>-saturated 1 M KOH electrolyte using a standard three-electrode system. The OER activities of NF, NiFe-LDH, and a series of NiFe sulfides (including NiFe-S, NiFe-S-0.2, NiFe-S-0.4, NiFe-S-0.6, NiFe-S-0.8, and NiFe-S-1.0) are compared in Fig. 4 and Fig. S9, in which the best OER performance catalyst was obtained with a 0.6 V treatment. As shown in Fig. 4a and Fig. S9, the NiFe-S-0.6 has the lowest overpotential of 213 mV at 10 mA cm<sup>-2</sup>, superior to other NiFe-based catalysts (NiFe-LDH-261 mV, NiFe-S-238 mV, NiFe-S-0.2-235 mV, NiFe-S-0.4-227 mV, NiFe-S-0.8-227 mV, NiFe-S-1.0-223 mV and commercial RuO<sub>2</sub> (312 mV) [30]), suggesting the indispensability of S and vacancy in effectively adjusting the adsorption and desorption of intermediate species O\* and OOH\* on catalyst's surface [44]. Besides, as shown in Fig. 4a, c, it is obvious that the current density growth rate of NiFe-S-0.6 with the increased potential is very fast ( $\eta_{100}$  = 252 mV,  $\eta_{500}$  = 294 mV, and  $\eta_{1000}$  = 304 mV), outperforming most of the previous studies on transition metal sulfides and vacancy-assisted catalysts shown in Table S1. Obviously, an inflection takes place at the current density of about 1500 mA cm<sup>-2</sup>, which is attributed to reaching the mass transfer and durability limitations at



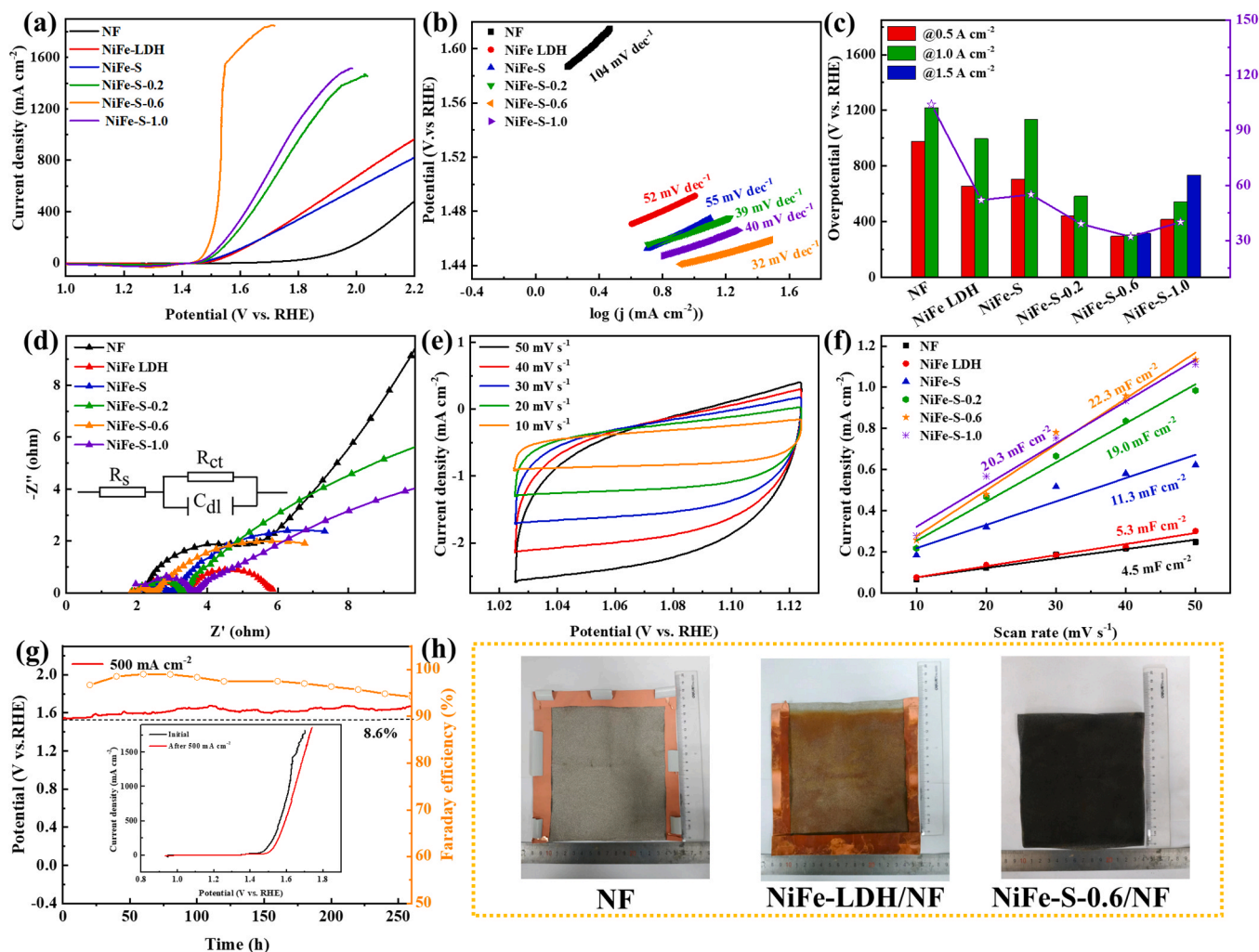


**Fig. 4.** (a) LSV curves, (b) Tafel slope, (c) overpotential at 0.5, 1.0, and 1.5 A cm<sup>-2</sup> and Tafel slopes, (d) EIS of NF, NiFe-LDH, NiFe-S, NiFe-S-0.2, NiFe-S-0.6, and NiFe-S-1.0 catalysts, (e) CV curves at different scan rates for NiFe-S-0.6, (f) ECSA of NF, NiFe-LDH, NiFe-S, NiFe-S-0.2, NiFe-S-0.6, and NiFe-S-1.0 catalysts, (g) potential-time (V-t) curves and Faradaic efficiency of NiFe-S-0.6/NF for 260 h (inset: LSV curves for pristine and OER tested NiFe-S-0.6/NF), (h) pictures for large area catalysts.

high current density [56], and a similar phenomenon also appears in high temperature and high-concentration electrolytes. Fig. 4b and Fig. S10c reveal the Tafel slopes of all as-prepared catalysts to illustrate the kinetic rate and catalytic mechanism during OER. NiFe-S-0.6 has a lower Tafel slope (32 mV dec<sup>-1</sup>) than NiFe-LDH (52 mV dec<sup>-1</sup>), NiFe-S (55 mV dec<sup>-1</sup>), NiFe-S-0.2 (39 mV dec<sup>-1</sup>), NiFe-S-0.4 (34 mV dec<sup>-1</sup>), NiFe-S-0.8 (34 mV dec<sup>-1</sup>) and NiFe-S-1.0 (40 mV dec<sup>-1</sup>), implying a fast kinetic process. Partially enlarged images of LSV with scanning from high voltage to low and low voltage to high are shown in Fig. S10a and Fig. S10b, where the cathodic and anodic peaks are caused by the reduction of Ni<sup>3+</sup> to Ni<sup>2+</sup> and the oxidation of Ni<sup>2+</sup> to Ni<sup>3+</sup> [57]. The NiFe-S-0.6 catalyst outperforms other catalysts in terms of OER performance, as evidenced by a larger REDOX area, more Ni<sup>3+</sup> to Ni<sup>2+</sup> reduction, and more Ni<sup>2+</sup> to Ni<sup>3+</sup> oxidation potential, indicating rich S vacancies can promote the formation of active NiOOH phases with changing electronic structure [58]. As shown by the Nyquist plots (Fig. 4d, S10d), NiFe-S-0.6 has the smallest resistance R<sub>ct</sub> (0.40 Ω) for charge transfer, which is smaller than that of the other catalysts (NiFe-LDH (3.68 Ω), NiFe-S (3.71 Ω), NiFe-S-0.2 (1.22 Ω), NiFe-S-0.4 (1.34 Ω), NiFe-S-0.8 (0.52 Ω), and NiFe-S-1 (1.33 Ω)). The EIS results reveal that NiFe-S-0.6 electrocatalyst processes a great conductivity and a fast electron transfer speed, which can effectively promote the OER process. Compared to LDH, the introduction of the S element can

enhance catalyst activity apparently [59]. In order to improve the OER performance of NiFe sulfide furthermore, an electrochemical reduction is adopted to create S vacancies for the adjustment of electronic structure and the effect of S vacancies is very significant. However, the clear change/turning point of NiFe-S-0.6 also cannot be neglected in terms of attenuation and catalyst loss over a current density of 1600 mA cm<sup>-2</sup>.

Moreover, the ECSA is a key factor to evaluate the real active area, which can be measured by calculating CV curves at different scan rates in the non-faraday region and noting the slope of the fitted line as C<sub>dl</sub> (Fig. 4e, f, S11, S12). The largest C<sub>dl</sub> occurring in NiFe-S-0.6 is 22.3 mF cm<sup>-2</sup> (Fig. 4f), illustrating the high specific surface area and numerous active sites coupled with the structural characteristic of the catalyst. However, C<sub>dl</sub> values of 21.0, 20.3, 19.0, 18.1, 11.3, and 5.3 mF cm<sup>-2</sup> occur with NiFe-S-0.8, 1.0, 0.2, 0.4, NiFe-S, and LDH, respectively. In addition, the ECSA can be calculated from the equation of ECSA = C<sub>dl</sub>/C<sub>s</sub>, and the specific capacitances (C<sub>s</sub>) are generally in the range of 20–60 μF cm<sup>-2</sup>, and here we use 40 μF cm<sup>-2</sup> based on the previous studies [60]. On this basis, the corresponding ECSA is 557.5 mF cm<sup>-2</sup> for NiFe-S-0.6. Stability is another vital assessment criterion for evaluating the electrocatalyst performance of catalysts. Stability tests generally use Chronopotentiometry experiments at a constant current density, which has been performed in this research with a current density of 500 mA cm<sup>-2</sup> at room temperature in 1 M KOH, and the result is shown in Fig. 4g. The



curve is almost flat for the first 20 h, then rises slowly, which means the reaction species are the original sulfides with rich vacancies and there is no reconstruction of catalyst at the first. After a 260 h OER test, the NiFe-S-0.6 potential has increased by 8.6%, but there are some fluctuations in the potential line (Fig. 4g). Meanwhile, as a result of the depletion of electrolyte required for the formation of hydrogen and oxygen and their evaporation during long-term OER tests, electrolyte supplements are indispensable. Our work adopted a constant flow injection pump to replenish electrolytes at a rate of  $0.1 \text{ mL h}^{-1}$ , which will actually cause the pool level to inevitably fluctuate. The inset of Fig. 4g shows the LSV of NiFe-S-0.6 before and after the 260 h OER test, in which the overpotential has slightly increased at the current density of  $500 \text{ mA cm}^{-2}$ , meaning NiFe-S-0.6 possesses excellent stability. It is noteworthy that there is no obvious inflection point in the LSV curve with the long-term stability test compared to the initial LSV, which may be attributed to the variety of catalysts. The orange curve in Fig. 4g presents the Faradaic efficiency of NiFe-S-0.6 in water splitting, and the Faraday efficiency can be maintained to 94.18% after 260 h of OER testing. We expect that Ni-Fe (oxy)hydroxide would form on the surface of NiFe-S-0.6 during OER. Remarkably, the electrodeposition-assisted IOE method is easily scaled up, allowing for the direct synthesis of large-scale catalysts for industrial applications. A large-area catalyst (about  $15 \times 16 \text{ cm}^2$ ) with a uniform NiFe-S-0.6 nanosheet array on NF has been created, as shown in Fig. 4h. The schematic of the double anode electrolyzer used to synthesize uniform NiFe-LDH on both sides is shown in Fig. S13a. A copper strip was placed on the NF's edge to weaken the edge effect of the electric field during the electrodeposition and electrochemical reduction processes (Fig. S13b). The price details of all of the chemicals and electrodes used in this experiment are listed in Fig. S13c, indicating that a large area catalyst can be synthesized for as low as \$20 and that the solution and electrodes can be reused. Specifically, the electrodeposition-assisted IOE method has the greatest potential for large-scale catalyst preparation and application to industrial hydrogen production.

The SEM image of catalysts after a long-term OER test is shown in Fig. 1f, indicating that the basic 3D skeleton morphology of NiFe-S-0.6 nanosheets has been well maintained, while some nanosheets aggregated and some have changed silhouette. At the same time, from the TEM of catalysts after long-term testing, the nanosheets can also be found (Fig. S6a) and the interplanar spaces of the inner part changed to 0.234 nm, and 0.199 nm (Fig. S6c) corresponding to (400) and (422) planes for  $(\text{Fe, Ni})_3\text{S}_4$ . However, the outer shell generally presents an amorphous structure or poor crystallinity. Fig. S6c still shows rich vacancies in the inner core, meaning the stability of sulfur vacancies in the bulk of the catalyst. Consequently, we certainly predict that the long-term oxygen production process generates some new substances. In order to further confirm the substances, the XPS measurement was performed for NiFe-S-0.6 after the OER durability test, as depicted in Fig. 3. From the Fe 2p spectrum of long-term tested NiFe-S-0.6 (Fig. 3a), the shapes and locations of peaks have completely changed, confirming that the new substance is iron (oxy)hydroxide [61]. Simultaneously, the proportion of  $\text{Fe}^{3+}$  has increased slightly, but the ratio of  $\text{Fe}^{2+}$  and  $\text{Fe}^{3+}$  is 1.24:1. The peaks of  $\text{Ni}^{3+}$  and  $\text{Ni}^{2+}$  have little variation in the XPS spectrum of Ni 2p, while the  $\text{Ni}^{3+}$  percentage and satellite peak area have increased after the OER durability test as shown in Fig. 3b. In general, the proportion of  $\text{Fe}^{2+}$  and  $\text{Ni}^{2+}$  is still more than that of  $\text{Fe}^{3+}$  and  $\text{Ni}^{3+}$ , demonstrating  $V_s$  would maintain stability even when subjected to a high oxidation voltage. Decreased  $\text{Ni}^{2+}$  or  $\text{Fe}^{2+}$  and increased  $\text{Ni}^{3+}$  or  $\text{Fe}^{3+}$  might encourage the formation of adsorbed O and OO intermediate species, thereby accelerating OER [62]. As can be seen at the top of Fig. 3c, the locations of S 2p<sub>1/2</sub> and S 2p<sub>3/2</sub> peaks for  $\text{S}^{2-}$  have been shifted to high binding energy, which is not far from that of NiFe-S after the 260 h OER durability test. The quantity of the S oxidation state is very much increased and the peak position moved to where they are close to that of NiFe-S, suggesting that the sulfide surface is oxidized to some extent. Moreover, peaks of Fe 2p and Ni 2p regions in XPS spectra

have been shifted to higher binding energy, further confirming the generation of corresponding metal oxysulfide [63]. Fig. S7b is the XPS spectrum of O1s for long-term tested NiFe-S-0.6, which demonstrates the existence of M-O and O-H bonds as well as the formation of metal oxysulfide. The full XPS spectrum for OER tested catalysts is shown in Fig. S7c while the XRD patterns of OER tested NiFe-S-0.6 are displayed in Fig. S7a, which show no obvious differences from the initial material and match the formation of amorphous oxysulfide. Based on the XPS, TEM, and XRD results discussed above, it is possible to confirm the formation of new amorphous nickel iron oxysulfide [64], which can be considered as the phase with truly active sites to boost OER.

In accordance with the result of electrochemical experiments and corresponding characterization tests, we postulate an appropriate oxygen evolution reaction mechanism, and the particulars are shown in Fig. 5a. Metal oxides are more thermodynamically stable than metal sulfides under the oxidizing potential from a solid-state chemical view [65]. We may expect sulfides would be easily oxidized to oxysulfide during the OER process [66], which also corresponds to the TEM (Fig. S6), XRD (Fig. S7a), and XPS (Fig. S7b,c) of the tested sample. In the OER process, the divalent metallic elements are oxidized to trivalent elements and a fresh oxysulfide is formed. The exposed fresh active sites will boost OER and exhibit outstanding stability under oxygen evolution conditions. Rich-vacancy metal sulfides tend to have more divalent metallic elements, which is advantageous for the in-situ generation of highly active and fresh oxysulfides. Specifically,  $V_s$  created by electro-reduction can exist stably in catalysts.

In short, all of the above results indicate the NiFe-S-0.6 nanosheets on the surface would be partially converted to Ni-Fe oxysulfides and form amorphous or metastable  $\text{NiFeO}_x\text{S}_y\text{H}/\text{NiFeS}$  heterojunction structure, which may be more active for electrocatalysis, while the nanosheet structure will be well-maintained during the OER process. Thus, NiFe-S-0.6 plays the role of pre-catalyst in the oxygen evolution process and behaves with excellent stability.

### 3.3. Role of sulfur vacancies and catalysis mechanism

In order to further understand the mechanism of electrocatalysts for enhancing oxygen evolution activity after introducing sulfur vacancies, the first-principles density functional theory (DFT) calculations were adopted [67], and a series intermediate adsorption Gibbs free energies ( $\Delta G$ ) of  $(\text{Fe, Ni})_3\text{S}_4$  and rich-sulfur vacancies  $(\text{Fe, Ni})_3\text{S}_4(V_s-(\text{Fe, Ni})_3\text{S}_4)$  were calculated. The specific theoretical calculation process is shown in the supporting information. Traditionally, a perfect OER electrocatalyst should have a desirable  $\Delta G$  for the adsorption and desorption of intermediates during OER. Fig. S14 shows the structures of (311), (400), (422) surfaces from the top and side view, and the (400) surface has the lowest surface energy with  $0.34 \text{ J m}^{-2}$ , indicating that the OER reaction is the most likely to take place on (400). So, the  $\Delta G$  of intermediates including  $^*\text{OH}$ ,  $^*\text{O}$ , and  $^*\text{OOH}$  on Fe and Ni sites in (400) surfaces of pristine  $(\text{Fe, Ni})_3\text{S}_4$  and  $V_s-(\text{Fe, Ni})_3\text{S}_4$  are obtained at conditions of  $U=0 \text{ V}$  and  $\text{pH}=14$ . As depicted in Fig. 5b, the most difficult step for both Ni and Fe active sites of pristine  $(\text{Fe, Ni})_3\text{S}_4$  is the conversion of  $^*\text{O}$  to  $^*\text{OOH}$ , which is considered the rate-determining step (RDS) [68] and needs higher reaction free energies of 2.86 eV and 3.10 eV, respectively. Comparing the free energy required to adsorb in each step, the Ni site is the main active site for oxygen evolution in pristine  $(\text{Fe, Ni})_3\text{S}_4$ . Significantly, introducing sulfur vacancies into  $(\text{Fe, Ni})_3\text{S}_4$ , the required free energy for the RDS of the Ni site is reduced to 2.42 eV, while the RDS of the Fe site has changed to the conversion step of  $^*\text{OOH}$  to  $\text{O}$ , which needs only 2.16 eV. Due to the lowest required free energy of each step, the main active site has translated to the Fe site after generating sulfur vacancies. Fig. 5a displays the structures of intermediates and the specific OER process at the Fe site with sulfur vacancies from a top view and Fig. S15 illustrates OER at the other active sites.

The charge density difference map [69] near the Fe site in  $V_s-(\text{Fe, Ni})_3\text{S}_4$  with adsorbed  $\text{H}_2\text{O}$  (Fig. 5c) revealed a more electrons cloud (the

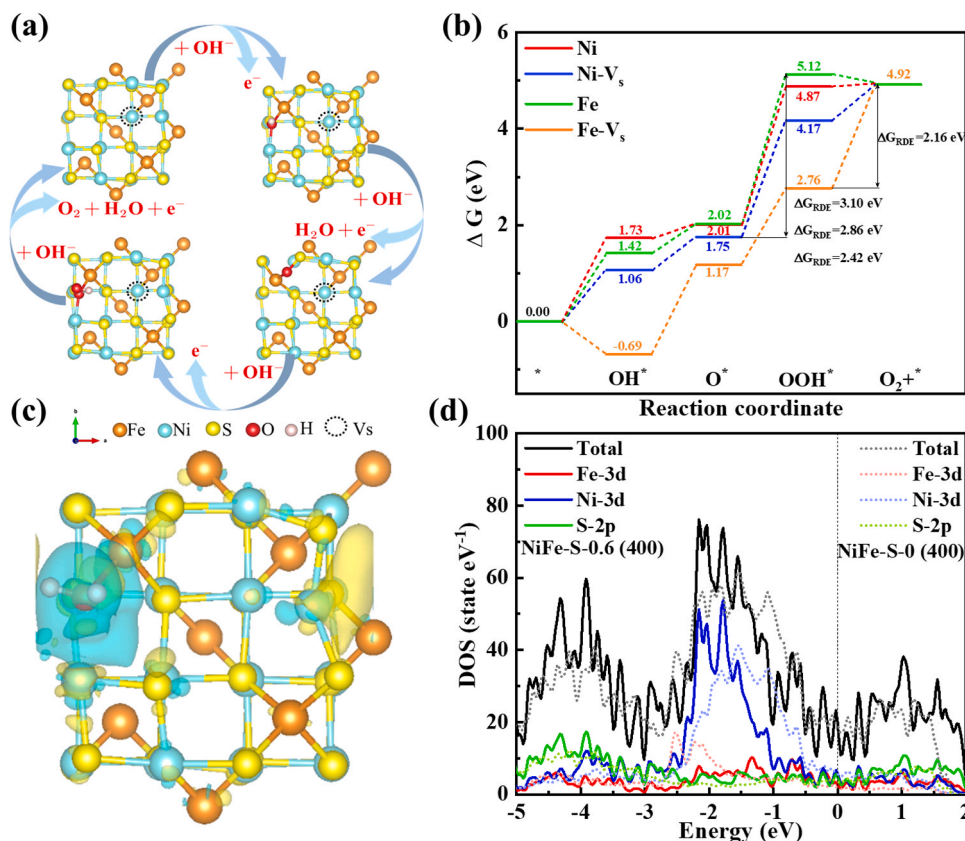


**Fig. 5.** (a) The top side of the adsorption energy model of  $V_s-(Fe, Ni)_3S_4$ , (b) Gibbs free energy profiles of  $(Fe, Ni)_3S_4$  and  $V_s-(Fe, Ni)_3S_4$  at Ni and Fe sites for OER at  $U=0$  and  $pH=14$ , (c) the charge density difference near Fe site in  $V_s-(Fe, Ni)_3S_4$  with adsorbed  $H_2O$  and (d) the total and Ni 3d, Fe 3d and S 2p DOS of  $(Fe, Ni)_3S_4$  and  $V_s-(Fe, Ni)_3S_4$ .

yellow iso-surface) around the Fe site and closer to it compared to the maps of the other active sites (as shown in Fig. S16), indicating Fe sites with sulfur vacancies adsorb  $H_2O$  easier or are more active, which agrees well with the results of required adsorption free energy. The density of state (DOS) analysis was also carried out to acquire the electronic property of pristine  $(Fe, Ni)_3S_4$  and  $V_s-(Fe, Ni)_3S_4$ . From Fig. 5d, a continuous DOS for both materials near the Fermi energy level means

the intrinsic metallic property [62]. In addition, the total DOS of pristine  $(Fe, Ni)_3S_4$  is weaker than that of  $V_s-(Fe, Ni)_3S_4$  near the Fermi energy level, reflecting that the electron conductivity for favorable electrons transfer and charge carrier density could be enhanced through introducing sulfur vacancies [45]. In total DOS curves, the Ni 3d and Fe 3d states mainly contribute to electronic interaction between the surface of catalysts and intermediates for both materials. The divided DOSs of Ni

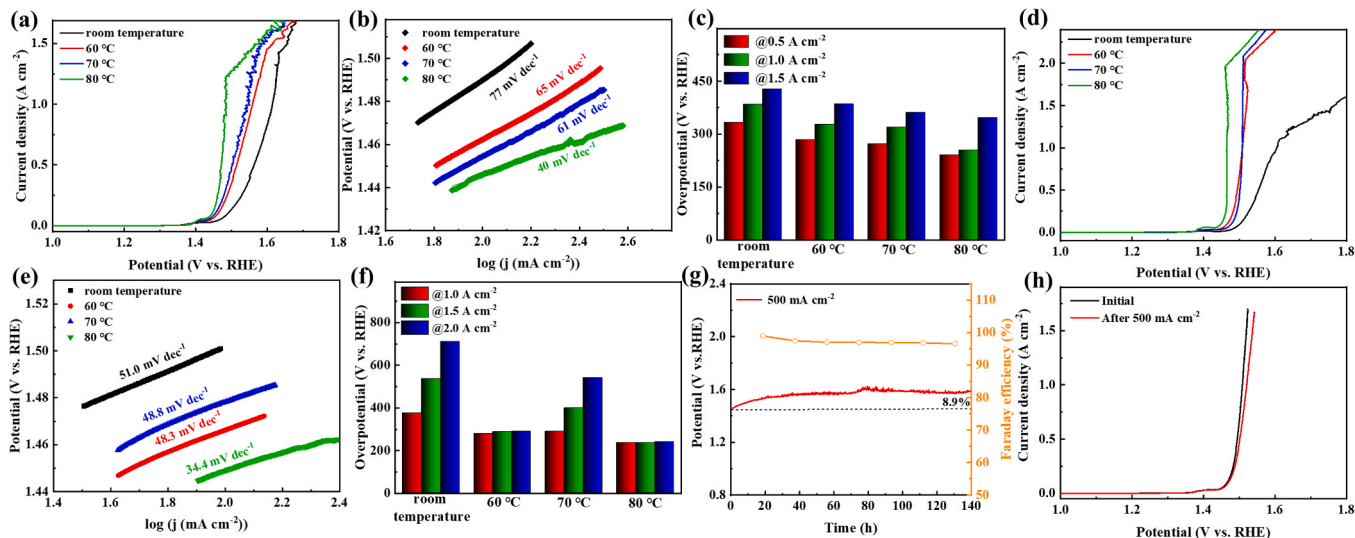


**Fig. 6.** (a) LSV curves, (b) Tafel slope, and (c) overpotential of NiFe-S-0.6 at different temperatures in 1 M KOH; (d) LSV curves, (e) Tafel slope, and (f) overpotential of NiFe-S-0.6 at different temperatures in 6 M KOH, (g) potential-time (V-t) curves and Faraday efficiency, (h) the LSV curves of pristine and OER tested of NiFe-S-0.6/NF at 60 in 6 M KOH solution.

3d and Fe 3d orbitals for  $V_s\text{-(Fe, Ni)}_3\text{S}_4$  have decreased compared to  $(\text{Fe, Ni})_3\text{S}_4$ , implying sulfur vacancies could reduce metallic atom energy and increase the ability to transfer electrons. The increased DOS of the S 2p orbital also indicates the enhanced activity of the reaction by creating sulfur vacancies in  $(\text{Fe, Ni})_3\text{S}_4$ .

In short, the results of DFT calculations further demonstrate that the created vacancies in NiFe sulfides would improve conductivity and modulate electronic structure to reach suitable adsorption or desorption states for intermediates, and finally enhance the oxygen evolution activity significantly.

### 3.4. Electrochemical performance in near industrial condition

We have carried out a series of experiments to determine the potential industrial application of NiFe-S-0.6 catalyst. Fig. 6a–d shows the electrochemical performance of NiFe-S-0.6 at different temperatures in 1 M KOH. In Fig. 6a, the relationship between OER capability and different temperatures is demonstrated via the LSV curves. With the raising of temperature, the current density can reach the higher place at the same voltage, and the best performance is shown at the operating temperature of 80 °C with an overpotential of 215 mV at 100 mA cm<sup>-2</sup>, while at 70 °C, 60 °C, and room temperature the overpotentials are 224 mV, 232 mV, and 252 mV, respectively. However, due to the faster decay in the microstructure of the catalyst, high temperature is detrimental to catalyst longevity at a high current density. Fig. 6b shows the Tafel slopes for different temperatures at high current densities, suggesting the fastest kinetic process at 80 °C. The overpotentials in this study (Fig. 6c) are 241 mV (0.5 A cm<sup>-2</sup>), 254 mV (1 A cm<sup>-2</sup>), and 346 mV (1.51 A cm<sup>-2</sup>) at 80 °C, which have exceeded the previously reported results and compared in Table S2. In summary, high temperatures (near industrial conditions) are favorable for OER performance at current densities of less than 1.5 A cm<sup>-2</sup>.

It is well-known that electrolyte concentration is also a crucial factor in OER. Traditionally, a 20–30 wt% KOH solution is used as the industrial electrolyte for the electrolysis of water. Here, we adopt a 6 M KOH solution to evaluate the electrochemical performance of the as-prepared electrocatalyst at different temperatures, and the results are shown in Fig. 6d–h. From the LSV curves as shown in Fig. 6d, all LSV curves have a very significant break point and the corresponding current densities are 1.97 A cm<sup>-2</sup> at 80 °C, 2.08 A cm<sup>-2</sup> at 70 °C, and 2.06 A cm<sup>-2</sup> at 60 °C, respectively. As current densities are increased above the breakpoints, catalytic performance deteriorated rapidly due to the limitations of mass transfer and poor mechanical stability of the catalyst [63,70]. However, the breakpoint of the catalysts tested at room temperature is as low as 1.2 A cm<sup>-2</sup> and causes great damage to the catalyst. The above results indicate that a high concentration of KOH will degrade the activity of catalysts, but raising the temperature to industrial levels can greatly improve catalyst performance. As the current density is adjusted to less than the breakpoint, the LSV curve presents a vertical-like curve and there is a small difference in the value of overpotentials (Fig. 6d,f). For example, as the temperature of the catalytic process is controlled at 80 °C, the NiFe-S-0.6 sample delivers an overpotential of 235 mV at 1000 mA cm<sup>-2</sup>, 237 mV at 1500 mA cm<sup>-2</sup> and 240 mV at 2000 mA cm<sup>-2</sup>. Compared to recently reported results by others (Table S2), the OER performance of this work has significantly outperformed most previous investigations under quasi-industrial conditions. In addition, the Tafel slopes (Fig. 6e) in the 6 M KOH solution are lower than that in 1 M KOH, suggesting the faster kinetics of the transfer process, and 80 °C may be considered as the optimal experimental parameter when only considering catalyst activity. Considering that the green hydrogen industry requires a current density of more than 200 mA cm<sup>-2</sup> and a temperature range of 60–80 °C, we carried out the Chronopotentiometry experiment in 6 M KOH solution for 140 h at 500 mA cm<sup>-2</sup> and 60 °C. As shown in Fig. 6g, the potential climbs up slowly in the initial 20 h, then almost no change occurs until the 70th hour. As a result, only 8.9% of the increased potential is observed.

Besides, the Faradaic efficiency of NiFe-S-0.6 catalyst still reached to 96.57% when it is applied for water splitting under industrial conditions, meaning high energy utilization. The LSV curves before and after the life test illustrate the small variation in the activity of catalysts, just as shown in Fig. 6h. Fig. 6g,h demonstrates that NiFe-S-0.6 catalyst has favorable stability at high current density in a strongly alkaline environment, indicating that it is useful for industrial application.

## 4. Conclusions

In summary, we have put forward a facile electrochemical reduction approach to create rich sulfur vacancies in nickel iron sulfide for the first time, greatly affecting electrocatalytic OER performance via regulating surface property and electronic structure. According to TEM, XRD, Raman, XPS, and XAS characterizations, we conclude that S vacancies are successfully generated through the electrochemical method. In 1 M KOH electrolytes, as prepared NiFe-S-0.6 catalyst demonstrated excellent OER activity with a low overpotential (213 mV at 10 mA cm<sup>-2</sup>) and a small Tafel slope (32 mV dec<sup>-1</sup>), and it also achieved long-term stability for 260 h while operating at a high current density (500 mA cm<sup>-2</sup>). The unique morphology of nanosheets with the formation of pores, as well as the adjusted appropriate electronic structure through vacancies, are responsible for astounding performance. Additionally, DFT calculations also show that vacancies improved catalyst conductivity, with Fe sites serving as the primary active sites. A new phase called oxysulfide could also emerge after a high current density OER test, maintaining sulfur vacancies and producing a high level of durability. Most importantly, we discovered that NiFe-S-0.6 has a substantially high alkaline tolerance (140 h at 500 mA cm<sup>-2</sup> in 6 M KOH) at the industrial temperature (60 °C) and a very low overpotential (235 mV at 1000 mA cm<sup>-2</sup>). Remarkably, the proposed technical route was used to effectively synthesize an electrocatalyst with an area of 15 × 16 cm<sup>2</sup>. Hence, we anticipate that this work will offer fresh insight into the utilization of sulfur vacancies in the production of hydrogen and will further open up the vast potential for electrochemical hydrogen production on an industrial scale.

### CRediT authorship contribution statement

**He Lixiang:** Investigation, Methodology, Data curation, Writing – original draft. **Wang Ni:** Conceptualization, Data curation, Supervision, Writing – review & editing. **Xiang Mingliang:** Writing – review & editing. **Zhong Li:** Writing – review & editing. **Komarneni Sridhar:** Writing – review & editing. **Hu Wencheng:** Conceptualization, Funding acquisition, Supervision, Writing – review & editing.

### Declaration of Competing Interest

The authors declare that they have no known competing financial interests or personal relationships that could have appeared to influence the work reported in this paper.

### Data Availability

Data will be made available on request.

### Acknowledgements

We acknowledge the funding support by the Sichuan Science and Technology Program (No. 2021YFH0186) and the National Natural Science Foundation of China (Grant No. 51902041). This theoretical calculation was carried out in part using computing resources at The National Supercomputing Center of Shenzhen.



## Appendix A. Supporting information

Supplementary data associated with this article can be found in the online version at [doi:10.1016/j.apcatb.2023.123686](https://doi.org/10.1016/j.apcatb.2023.123686).

## References

- [1] M. Retuerto, L. Pascual, J. Torroero, M.A. Salam, T.M. Álvaro, D. Gianolio, P. Ferrer, P. Kayser, V. Wilke, S. Stiber, V. Celorrio, M. Mokhtar, D.G. Sanchez, A.S. Gago, K. A. Friedrich, M.A. Peña, J.A. Alonso, S. Rojas, Highly active and stable OER electrocatalysts derived from  $\text{Sr}_2\text{MnO}_6$  for proton exchange membrane water electrolyzers, *Nat. Commun.* 13 (2022) 7935, <https://doi.org/10.1038/s41467-022-35631-5>.
- [2] Q. Wu, X. Yang, J. Yang, P. Liu, G. Ding, Z. Chen, G. Liao, Size effect of ruthenium nanoparticles on water cracking properties with different crystal planes for boosting electrocatalytic hydrogen evolution, *J. Colloid Interf. Sci.* 644 (2023) 238–245, <https://doi.org/10.1016/j.jcis.2023.04.076>.
- [3] Y. Zhai, X. Ren, Y. Sun, D. Li, B. Wang, S. Liu, Synergistic effect of multiple vacancies to induce lattice oxygen redox in NiFe-layered double hydroxide OER catalysts, *Appl. Catal. B-Environ.* 323 (2023) 122091, <https://doi.org/10.1016/j.apcatb.2022.122091>.
- [4] T.-Y. Shuai, Q.-N. Zhan, H.-M. Xu, Z.-J. Zhang, G.-R. Li, Recent developments of MXene-based catalysts for hydrogen production by water splitting, *Green. Chem.* 25 (2023) 1749–1789, <https://doi.org/10.1039/D2GC04205C>.
- [5] L. Zhong, L. He, N. Wang, Y. Chen, X. Xie, B. Sun, J. Qian, S. Komarneni, W. Hu, Preparation of metal-organic framework from in situ self-sacrificial stainless-steel matrix for efficient water oxidation, *Appl. Catal. B-Environ.* 325 (2022) 122343, <https://doi.org/10.1016/j.apcatb.2022.122343>.
- [6] T. He, Y. Chen, Q. Liu, B. Lu, X. Song, H. Liu, M. Liu, Y.N. Liu, Y. Zhang, X. Ouyang, S. Chen, High-density cationic defects coupling with local alkaline-enriched environment for efficient and stable water oxidation, *Angew. Chem. Int. Ed.* 135 (2023) e202217815, <https://doi.org/10.1002/anie.20220100>.
- [7] L. He, G. Yu, Y. Cheng, N. Wang, W. Hu, Non-precious metal-based catalysts for water electrolysis to produce  $\text{H}_2$  under industrial conditions, *Mater. Chem. Front.* 7 (2023) 5661–5692, <https://doi.org/10.1039/D3QM00557G>.
- [8] T. Wang, P. Wang, W. Zang, X. Li, D. Chen, Z. Kou, S. Mu, J. Wang, Nanoframes of  $\text{Co}_3\text{O}_4$ - $\text{Mo}_2\text{N}$  heterointerfaces enable high-performance bifunctionality toward both electrocatalytic HER and OER, *Adv. Funct. Mater.* 32 (2022) 2107382, <https://doi.org/10.1002/adfm.202107382>.
- [9] Q. Wang, H. Xu, X. Qian, G. He, H. Chen, Oxygen and sulfur dual vacancy engineering on a 3D  $\text{Co}_3\text{O}_4/\text{Co}_2\text{S}_4$  heterostructure to improve overall water splitting activity, *Green. Chem.* 24 (2022) 9220–9232, <https://doi.org/10.1039/D2GC03315A>.
- [10] J. Bak, T.G. Yun, J.S. An, H.B. Bae, S.Y. Chung, Comparison of Fe-enhanced oxygen evolution electrocatalysis in amorphous and crystalline nickel oxides to evaluate the structural contribution, *Energ. Environ. Sci.* 15 (2022) 610–620, <https://doi.org/10.1039/D1EE01826D>.
- [11] J. Mei, J. Shang, T. He, D. Qi, L. Kou, T. Liao, A. Du, Z. Sun, 2D/2D black phosphorus/nickel hydroxide heterostructures for promoting oxygen evolution via electronic structure modulation and surface reconstruction, *Adv. Energy Mater.* 12 (2022) 211141, <https://doi.org/10.1002/aenm.202201141>.
- [12] P. Thangavel, G. Kim, K.S. Kim, Electrochemical integration of amorphous NiFe (oxy)hydroxides on surface-activated carbon fibers for high-efficiency oxygen evolution in alkaline anion exchange membrane water electrolysis, *J. Mater. Chem. A* 9 (2021) 14043–14051, <https://doi.org/10.1039/D1TA02883A>.
- [13] L. He, N. Wang, B. Sun, L. Zhong, M. Yao, W. Hu, S. Komarneni, High-entropy FeCoNiMn (oxy)hydroxide as high-performance electrocatalyst for OER and boosting clean carrier production under quasi-industrial condition, *J. Clean. Prod.* 356 (2022) 131680, <https://doi.org/10.1016/j.jclepro.2022.131680>.
- [14] R.C. Rohit, A.D. Jagadale, S.K. Shinde, D.Y. Kim, A review on electrodeposited layered double hydroxides for energy and environmental applications, *Mater. Today Commun.* 27 (2021) 102275, <https://doi.org/10.1016/j.mtcomm.2021.102275>.
- [15] H.-J. Yin, J.-H. Zhou, Y.-W. Zhang, Shaping well-defined noble-metal-based nanostructures for fabricating high-performance electrocatalysts: advances and perspectives, *Inorg. Chem. Front.* 6 (2019) 2582–2618, <https://doi.org/10.1039/C9QI00689C>.
- [16] J. Chen, H. Li, S. Chen, J. Fei, C. Liu, Z. Yu, K. Shin, Z. Liu, L. Song, G. Henkelman, L. Wei, Y. Chen, Co-Fe-Cr (oxy)hydroxides as efficient oxygen evolution reaction catalysts, *Adv. Energy Mater.* 11 (2021) 2003412, <https://doi.org/10.1002/aenm.202003412>.
- [17] J. Liu, S. Liu, F. Yan, Z. Wen, W. Chen, X. Liu, Q. Liu, J. Shang, R. Yu, D. Su, J. Shui, Ultrathin nanotube structure for mass-efficient and durable oxygen reduction reaction catalysts in PEM fuel cells, *J. Am. Chem. Soc.* 144 (2022) 19106–19114, <https://doi.org/10.1021/jacs.2c08361>.
- [18] L. Wu, X. Shen, Z. Ji, J. Yuan, S. Yang, G. Zhu, L. Chen, L. Kong, H. Zhou, Facile synthesis of medium-entropy metal sulfides as high-efficiency electrocatalysts toward oxygen evolution reaction, *Adv. Funct. Mater.* 33 (2023) 2208170, <https://doi.org/10.1002/adfm.202208170>.
- [19] Y. Xin, F. Wang, L. Chen, Y. Li, K. Shen, Superior bifunctional cobalt/nitrogen-codoped carbon nanosheet arrays on copper foam enable stable energy-saving hydrogen production accompanied with glucose upgrading, *Green. Chem.* 24 (2022) 6544–6555, <https://doi.org/10.1039/D2GC02426H>.
- [20] A. Hameed, M. Batool, Z. Liu, M.A. Nadeem, R. Jin, Layered double hydroxide-derived nanomaterials for efficient electrocatalytic water splitting: Recent progress and future perspective, *ACS Energy Lett.* 7 (2022) 3311–3328, <https://doi.org/10.1021/acseenergylett.2c01362>.
- [21] J. Wang, J. Huang, G. Chen, W. Chen, T. Li, A. Meng, K. Ostrikov, In-situ engineered heterostructured nickel telluride nanosheets for robust overall water splitting, *Chem. Eng. J.* 446 (2022) 137297, <https://doi.org/10.1016/j.cej.2022.137297>.
- [22] S. Li, B. Chen, Y. Wang, M.Y. Ye, P.A. van Aken, C. Cheng, Oxygen-evolving catalytic atoms on metal carbides, *A. Thomas, Nat. Mater.* 20 (2021) 1240–1247, <https://doi.org/10.1038/s41563-021-01006-2>.
- [23] C.H. Lai, M.Y. Lu, L.J. Chen, Metal sulfide nanostructures: synthesis, properties and applications in energy conversion and storage, *J. Mater. Chem.* 22 (2012) 19–30, <https://doi.org/10.1039/C1JM13879K>.
- [24] X. Li, Z. Kou, S. Xi, W. Zang, T. Yang, L. Zhang, J. Wang, Porous  $\text{NiCo}_2\text{S}_4/\text{FeOOH}$  nanowire arrays with rich sulfide/hydroxide interfaces enable high OER activity, *Nano Energy* 78 (2020) 105230, <https://doi.org/10.1016/j.nanoen.2020.105230>.
- [25] F. Lyu, Q. Wang, S.M. Choi, Y. Yin, Noble-metal-free electrocatalysts for oxygen evolution, *Small* 15 (2019) 1804201, <https://doi.org/10.1002/smll.201804201>.
- [26] R. Luo, Z. Qian, L. Xing, C. Du, G. Yin, S. Zhao, L. Du, Re-looking into the active moieties of metal X-ides (X = phosph-, sulf-, nit-, and carb-) toward oxygen evolution reaction, *Adv. Funct. Mater.* 31 (2021) 212918, <https://doi.org/10.1002/adfm.202102918>.
- [27] X. Liu, J. Meng, J. Zhu, M. Huang, B. Wen, R. Guo, L. Mai, Comprehensive understandings into complete reconstruction of precatalysts: synthesis, applications, and characterizations, *Adv. Mater.* 33 (2021) 2007344, <https://doi.org/10.1002/adma.202007344>.
- [28] X. Xu, Y. Xu, Y. Liang, H. Long, D. Chen, H. Hu, J.Z. Ou, Vacancy-modified g- $\text{C}_3\text{N}_4$  and its photocatalytic applications, *Mater. Chem. Front.* 6 (2022) 3143–3173, <https://doi.org/10.1039/D2QM00604A>.
- [29] A.T. Garcia-Esparza, S. Park, H. Abroshan, O.A.P. Mellone, J. Vinson, B. Abraham, T.R. Kim, D. Nordlund, A. Gallo, R. Alonso-Mori, X. Zheng, D. Sokaras, Local structure of sulfur vacancies on the basal plane of monolayer  $\text{MoS}_2$ , *ACS Nano* 16 (2022) 6725–6733, <https://doi.org/10.1021/acsnano.2c01388>.
- [30] S. Liu, C. Che, H. Jing, J. Zhao, X. Mu, S. Zhang, C. Chen, S. Mu, Phosphorus-triggered synergy of phase transformation and chalcogenide vacancy migration in cobalt sulfide for an efficient oxygen evolution reaction, *Nanoscale* 12 (2020) 3129–3134, <https://doi.org/10.1039/C9NR90203J>.
- [31] F. Ye, S. Zhang, Q. Cheng, Y. Long, D. Liu, R. Paul, Y. Fang, Y. Su, L. Qu, L. Da, C. Hu, The role of oxygen-vacancy in bifunctional indium oxyhydroxide catalysts for electrochemical coupling of biomass valorization with  $\text{CO}_2$  conversion, *Nat. Commun.* 14 (2023) 2040, <https://doi.org/10.1038/s41467-023-37679-3>.
- [32] F. Rao, G. Zhu, W. Zhang, J. Gao, F. Zhang, Y. Huang, M. Hojamberdiev, In-situ generation of oxygen vacancies and metallic bismuth from  $(\text{BiO})_2\text{CO}_3$  via  $\text{N}_2$ -assisted thermal-treatment for efficient selective photocatalytic NO removal, *Appl. Catal. B-Environ.* 281 (2021) 119481, <https://doi.org/10.1016/j.apcatb.2020.119481>.
- [33] Q. Wu, W. Yang, X. Wang, W. Zhu, S. Lv, Y. Zhou, T. Chen, S. Liu, W. Li, Z. Chen, Inherent vacancy of compressive Ru nanoparticles accelerate electro-catalytic hydrogen energy conversion, *Appl. Catal. B-Environ.* 335 (2023) 122896, <https://doi.org/10.1016/j.apcatb.2023.122896>.
- [34] Y. Du, B. Zhang, W. Zhou, R. Kang, W. Zhang, H. Jin, J. Wan, J. Qin, J. Zhang, G. Chen, Laser-radiated tellurium vacancies enable high-performance telluride molybdenum anode for aqueous zinc-ion batteries, *Energy Storage Mater.* 51 (2022) 29–37, <https://doi.org/10.1016/j.ensm.2022.06.015>.
- [35] X. Chu, Y. Liao, L. Wang, J. Li, H. Xu, Engineering sulfur vacancies for boosting electrocatalytic reactions, *Chin. Chem. Lett.* 5 (2023) 108285, <https://doi.org/10.1016/j.ccllet.2023.108285>.
- [36] B. Ravel, M. Newville, ATHENA, ARTEMIS, HEPHAESTUS: data analysis for X-ray absorption spectroscopy using IFEFFIT, *J. Synchrotron Radiat.* 12 (2005) 537–541, <https://doi.org/10.1107/S0909049505012719>.
- [37] M. Xiang, L. He, N. Wang, J. Chen, W. Hu, Hydrothermally etching commercial carbon cloth to form a porous structure for flexible zinc-ion hybrid supercapacitors, *Appl. Surf. Sci.* 613 (2023) 156093, <https://doi.org/10.1016/j.apsusc.2022.156093>.
- [38] S. Huang, Z. Jin, P. Ning, C. Gao, Y. Wu, X. Liu, P. Xin, Z. Chen, Y. Jiang, Z. Hu, Z. Chen, Synergistically modulating electronic structure of  $\text{NiS}_2$  hierarchical architectures by phosphorus doping and sulfur-vacancies defect engineering enables efficient electrocatalytic water splitting, *Chem. Eng. J.* 420 (2021) 127630, <https://doi.org/10.1016/j.cej.2020.127630>.
- [39] J. Zhang, B. Shen, Z. Hu, M. Zhen, S.Q. Guo, F. Dong, Uncovering the synergy between Mn substitution and O vacancy in  $\text{ZnAl-LDH}$  photocatalyst for efficient toluene removal, *Appl. Catal. B-Environ.* 296 (2021) 120376, <https://doi.org/10.1016/j.apcatb.2021.120376>.
- [40] X. Guo, Z. Liu, F. Liu, J. Zhang, L. Zheng, Y. Hu, J. Mao, H. Liu, Y. Xue, C. Tang, Sulfur vacancies-tailored  $\text{NiCo}_2\text{S}_4$  nanosheet arrays for hydrogen evolution reaction at all pH values, *Catal. Sci. Technol.* 4 (2020) 1056–1065, <https://doi.org/10.1039/C9CY02189B>.
- [41] Y. Zhang, Z. Mu, C. Yang, Z. Xu, S. Zhang, X. Zhang, Y. Li, J. Lai, Z. Sun, Y. Yang, Y. Chao, C. Li, X. Ge, W. Yang, S. Guo, Rational design of MXene/ $^1\text{T}-^2\text{H}$   $\text{MoS}_2$ -C nanohybrids for high-performance lithium-sulfur batteries, *Adv. Funct. Mater.* 28 (2018) 1707578, <https://doi.org/10.1002/adfm.201707578>.
- [42] J. Chang, S. Zang, F. Song, W. Wang, D. Wu, F. Xu, K. Jiang, Z. Gao, Heterostructured nickel, iron sulfide@nitrogen, sulfur co-doped carbon hybrid with efficient interfacial charge redistribution as bifunctional catalyst for water

- electrolysis, *Appl. Catal. A-Gen.* 630 (2022) 118459, <https://doi.org/10.1016/j.apcata.2021.118459>.
- [43] D. Lim, C. Lim, M. Hwang, M. Kim, S.E. Shim, S.H. Baeck, Facile synthesis of flower-like P-doped nickel-iron disulfide microspheres as advanced electrocatalysts for the oxygen evolution reaction, *J. Power Sources* 490 (2021) 229552, <https://doi.org/10.1016/j.jpowsour.2021.229552>.
- [44] Y.N. Zhou, W.L. Yu, Y.N. Cao, J. Zhao, B. Dong, Y. Ma, F.L. Wang, R.Y. Fan, Y. L. Zhou, Y.M. Chai, S-doped nickel-iron hydroxides synthesized by room-temperature electrochemical activation for efficient oxygen evolution, *Appl. Catal. B-Environ.* 292 (2021) 120150, <https://doi.org/10.1016/j.apcatb.2021.120150>.
- [45] L. Yu, L. Wu, B. McElhenny, S. Song, D. Luo, F. Zhang, Y. Yu, S. Chen, Z. Ren, Ultrafast room-temperature synthesis of porous S-doped Ni/Fe (oxy)hydroxide electrodes for oxygen evolution catalysis in seawater splitting, *Energ. Environ. Sci.* 13 (2020) 3439–3446, <https://doi.org/10.1039/D0EE00921K>.
- [46] S. Li, C. Xi, Y.Z. Jin, D. Wu, J.Q. Wang, T. Liu, H.B. Wang, C.K. Dong, H. Liu, S. A. Kulnich, X.W. Du, Ir-O-V catalytic group in Ir-doped NiV(OH)<sub>2</sub> for overall water splitting, *ACS Energy Lett.* 4 (2018) 1823–1829, <https://doi.org/10.1021/acscenergylett.9b01252>.
- [47] H. Sun, J.M. Yang, J.G. Li, Z. Li, X. Ao, Y.Z. Liu, Y. Zhang, Y. Li, C. Wang, J. Tang, Synergistic coupling of NiTe nanoarrays with RuO<sub>2</sub> and NiFe-LDH layers for high-efficiency electrochemical-/photovoltage-driven overall water splitting, *Appl. Catal. B-Environ.* 272 (2020) 118988, <https://doi.org/10.1016/j.apcatb.2020.118988>.
- [48] K. Wan, J. Luo, C. Zhou, T. Zhang, J. Arbiol, X. Lu, B.W. Mao, X. Zhang, J. Fransaer, Hierarchical porous Ni<sub>3</sub>S<sub>4</sub> with enriched high-valence Ni sites as a robust electrocatalyst for efficient oxygen evolution reaction, *Adv. Funct. Mater.* 29 (2018) 1900315, <https://doi.org/10.1002/adfm.201900315>.
- [49] J. Tang, X. Jiang, L. Tang, Y. Li, Q. Zheng, Y. Huo, D. Lin, Self-supported wire-in-plate NiFeS/CoS nanohybrids with a hierarchical structure for efficient overall water splitting, *Dalton T.* 50 (2021) 5921–5930, <https://doi.org/10.1039/D1DT00319D>.
- [50] P. Ganesan, A. Sivanantham, S. Shanmugam, Inexpensive electrochemical synthesis of nickel iron sulphides on nickel foam: super active, ultra-durable electrocatalysts for alkaline electrolyte membrane water electrolysis, *J. Mater. Chem. A* 4 (2016) 16394–16402, <https://doi.org/10.1039/C6TA04499A>.
- [51] Z. Jing, Q. Zhao, D. Zheng, L. Sun, J. Geng, Q. Zhou, J. Lin, Nickel-doped pyrrhotite iron sulfide nanosheets as highly efficient electrocatalysts for water splitting, *J. Mater. Chem. A* 8 (2020) 20323–20330, <https://doi.org/10.1039/D0TA07624D>.
- [52] H. Fei, R. Liu, J. Wang, T. Guo, Z. Wu, D. Wang, F. Liu, Targeted modulation of competitive active sites toward nitrogen fixation via sulfur vacancy engineering over MoS<sub>2</sub>, *Adv. Funct. Mater.* 33 (2023) 2302501, <https://doi.org/10.1002/adfm.202302501>.
- [53] K. Jiang, M. Luo, Z. Liu, M. Peng, D. Chen, Y.-R. Lu, T.-S. Chan, F.M.F. de Groot, Y. Tan, Rational strain engineering of single-atom ruthenium on nanoporous MoS<sub>2</sub> for highly efficient hydrogen evolution, *Nat. Commun.* 12 (2021) 4687, <https://doi.org/10.1038/s41467-021-21956-0>.
- [54] K. Zeng, Y. Li, M. Tian, C. Wei, J. Yan, M.H. Rummeli, P. Strasser, R. Yang, Molybdenum-leaching induced rapid surface reconstruction of amorphous/crystalline heterostructured trimetal oxides pre-catalyst for efficient water splitting and Zn-air batteries, *Energy Storage Mater.* 60 (2023) 102806, <https://doi.org/10.1016/j.ensm.2023.102806>.
- [55] Y. Zhang, C. Ma, C. Zhang, L. Ma, S. Zhang, Q. Huang, C. Liang, L. Chen, L. Zhou, W. Wei, Selective catalysis of single V atoms and VN<sub>1-x</sub> nanodots enables fast polysulfides conversion in lithium-sulfur batteries, *Chem. Eng. J.* 452 (2023) 139410, <https://doi.org/10.1016/j.cej.2022.139410>.
- [56] Q. Wen, Y. Zhao, Y. Liu, H. Li, T. Zhai, Ultrahigh-current-density and long-term-durability electrocatalysts for water splitting, *Small* 18 (2022) 2104513, <https://doi.org/10.1002/smll.202104513>.
- [57] Y. Lin, H. Wang, C.K. Peng, L. Bu, C.L. Chiang, K. Tian, Y. Zhao, J. Zhao, Y.G. Lin, J. M. Lee, L. Gao, Co-induced electronic optimization of hierarchical NiFe LDH for oxygen evolution (<https://doi.org/>), *Small* 16 (2020) 2002426, <https://doi.org/10.1002/smll.202002426>.
- [58] M.K. Bates, Q. Jia, H. Doan, W. Liang, S. Mukerjee, Charge-transfer effects in Ni-Fe and Ni-Fe-Co mixed-metal oxides for the alkaline oxygen evolution reaction, *ACS Catal.* 6 (2016) 155–161, <https://doi.org/10.1021/acscatal.5b01481>.
- [59] R. Guo, H. Wen, S. Zhang, T. Yu, Y. He, Z. Ni, J. You, Anionic sulfur-modified FeNi-LDH at various Fe/Ni molar ratios for high-performance OER electrocatalysis, *Mater. Lett.* 285 (2021) 129132, <https://doi.org/10.1016/j.matlet.2020.129132>.
- [60] Y. Wu, Y. Li, M. Yuan, H. Hao, X. San, Z. Lv, L. Xu, B. Wei, Operando capturing of surface self-reconstruction of Ni<sub>3</sub>S<sub>2</sub>/FeNi<sub>2</sub>S<sub>4</sub> hybrid nanosheet array for overall water splitting, *Chem. Eng. J.* 427 (2022) 131944, <https://doi.org/10.1016/j.cej.2021.131944>.
- [61] B. Wang, S. Jiao, Z. Wang, M. Lu, D. Chen, Y. Kang, G. Pang, S. Feng, Rational design of NiFe LDH@Ni<sub>3</sub>N nano/microsheet arrays as a bifunctional electrocatalyst for overall water splitting, *J. Mater. Chem. A* 8 (2020) 17202–17211, <https://doi.org/10.1039/D0TA01966F>.
- [62] B. Fei, Z. Chen, J. Liu, H. Xu, X. Yan, H. Qing, M. Chen, R. Wu, Ultrathinning nickel sulfide with modulated electron density for efficient water splitting, *Adv. Energy Mater.* 10 (2020) 2001963, <https://doi.org/10.1002/aenm.202001963>.
- [63] C.X. Zhao, J.N. Liu, C. Wang, J. Wang, L. Song, B.Q. Li, Q. Zhang, An anionic regulation mechanism for the structural reconstruction of sulfide electrocatalysts under oxygen evolution conditions, *Energ. Environ. Sci.* 15 (2022) 3257–3264, <https://doi.org/10.1039/D2EE01036D>.
- [64] Q. Wu, S. Wang, J. Guo, X. Feng, H. Li, S. Lv, Y. Zhou, Z. Chen, Insight into sulfur and iron effect of binary nickel-iron sulfide on oxygen evolution reaction, *Nano Res.* 15 (2022) 1901–1908, <https://doi.org/10.1007/s12274-021-3800-6>.
- [65] B.R. Wygant, K. Kawashima, C.B. Mullins, An anionic regulation mechanism for the structural reconstruction of sulfide electrocatalysts under oxygen evolution conditions, *ACS Energy Lett.* 3 (2018) 2956–2966, <https://doi.org/10.1021/acscenergylett.8b01774>.
- [66] S. Jin, Are metal chalcogenides, nitrides, and phosphides oxygen evolution catalysts or Bifunctional catalysts? *ACS Energy Lett.* 2 (2017) 1937–1938, <https://doi.org/10.1021/acscenergylett.7b00679>.
- [67] Z. Liu, B. Tang, X. Gu, H. Liu, L. Feng, Selective structure transformation for NiFe/NiFe<sub>2</sub>O<sub>4</sub> embedded porous nitrogen-doped carbon nanosphere with improved oxygen evolution reaction activity, *Chem. Eng. J.* 395 (2020) 125170, <https://doi.org/10.1016/j.cej.2020.125170>.
- [68] N. Zhang, Y. Hu, L. An, Q. Li, J. Yin, J. Li, R. Yang, M. Lu, S. Zhang, P. Xi, C.H. Yan, Surface activation and Ni-S stabilization in NiO/NiS<sub>2</sub> for efficient oxygen evolution reaction, *Angew. Chem. Int. Ed.* 61 (2022) e202207217, <https://doi.org/10.1002/anie.202207217>.
- [69] M. Cui, C. Yang, B. Li, Q. Dong, M. Wu, S. Hwang, H. Xie, X. Wang, G. Wang, L. Hu, High-entropy metal sulfide nanoparticles promise high-performance oxygen evolution reaction, *Adv. Energy Mater.* 11 (2021) 2002887, <https://doi.org/10.1002/aenm.202002887>.
- [70] L. He, N. Wang, B. Sun, L. Zhong, Y. Wang, S. Komarneni, W. Hu, A low-cost and efficient route for large-scale synthesis of NiCoS<sub>x</sub> nanosheets with abundant sulfur vacancies towards quasi-industrial electrocatalytic oxygen evolution, *J. Colloid Interf. Sci.* 650 (2023) 1274–1284, <https://doi.org/10.1016/j.jcis.2023.07.084>.